Available online at www.sciencedirect.com
ScienceDirect
Catalysis Today 126 (2007) 303–312
CATALYSIS TODAY
www.elsevier.com/locate/cattod

The SMSI between supported platinum and CeO_2–ZrO_2–La_2O_3 mixed oxides in oxidative atmosphere

Jun Fan, Xiaodong Wu, Lei Yang, Duan Weng *

Department of Materials Science and Engineering, Tsinghua University, Beijing 100084, China

Available online 20 July 2007

Abstract

CeO_2–ZrO_2–La_2O_3 (CZL) mixed oxides were prepared by citric acid sol–gel method. The as-received gel was calcined at 500, 700, 900 and 1050 °C to obtain the so-called C5, C7, C9 and CK, respectively. The C5, C7 and C9 powders were impregnated with H_2PtCl_6 and then calcined at 500 °C to prepare P5C5, P5C7 and P5C9, respectively. The impregnated CK powders were calcined at 500, 700 and 900 °C to prepare P5CK, P7CK and P9CK, respectively. The XRD and XPS analyses show that the surface distribution of Pt is evidently influenced by the structural and textural properties of the support. The CO adsorption followed by FTIR reveals that the dispersion and the chemisorption sites of Pt are reduced as the calcination temperature of CZL support increases. The chemisorption ability of the CK samples is even completely deactivated. The encapsulation mechanism, which has been applied to explain the so-called strong metal–support interaction (SMSI) after reductive treatment, is introduced here to demonstrate the abnormal observations though the samples were prepared in oxidative atmosphere. The HRTEM results also confirm this explanation. The effects of oxygen vacancies, the chemisorption sites on the Pt surface and Pt/Ce interfacial sites on the three-way catalytic activities are discussed.

Keywords: Pt; CeO_2–ZrO_2–La_2O_3 mixed oxides; Distribution; Chemisorption site; Encapsulation

1. Introduction

On the basis of outstanding oxygen storage capacity (OSC) after sintering, CeO_2–ZrO_2 mixed oxides have been applied to replace ceria in three-way catalysts (TWC) [1–4]. Due to stringent legislations concerning automotive exhaust emissions, many efforts have been paid to improvements of OSC and thermal stability of CeO_2–ZrO_2. As the most common method, the doping of tri- or bi-valent cations has been widely investigated. For example, by incorporation of Ga^{3+}, Y^{3+} and La^{3+} into the $Ce_{0.6}Zr_{0.4}O_2$ lattice, an increased OSC by about 30% after a low temperature reduction was observed [5]. Moreover, the addition of low-valent dopants, such as La^{3+} and Y^{3+}, to CeO_2–ZrO_2 was reported to be efficient in restraining the undesirable segregation of Ce-rich and Zr-rich phase, which may occur upon high temperature calcinations [6].

Meanwhile, the precious metals serving as the active component in conventional TWCs have drawn much attention for their prominent promotion on the performances of the NM/CeO_2–ZrO_2 (NM = Pt, Rh and Pd) catalysts at low temperatures. In particular, a so-called strong metal–support interaction (SMSI), which is considered to remarkably affect the microstructure and properties of catalysts, has been focused on by many studies [7–10]. Liotta et al. [7] summarized the explanations which had been given for the influence of oxidative/reductive treatments on the activity of the Pt catalyst supported on CeO_2 or CeO_2–ZrO_2 by impregnation method: (i) alloy formation between Pt and Ce (when the reduction temperature T_{red} is higher than 900 °C); (ii) decoration or encapsulation of Pt by partially reduced ceria ($500 \leq T_{red} < 900$ °C) and (iii) pure electronic interactions ($T_{red} < 500$ °C). As summarized in the literatures [8,11], the characteristics of SMSI indicate that reductive treatments are emphatically required to induce this effect. However, it is well-known that catalysts can be aged in artificial way by high temperature treatment and/or exposure to strong reductive or oxidative atmosphere [12]. Considering the practical working

* Corresponding author. Tel.: +86 10 62772726; fax: +86 10 62772726.
E-mail address: duanweng@tsinghua.edu.cn (D. Weng).

0920-5861/$ – see front matter © 2007 Elsevier B.V. All rights reserved.
doi:10.1016/j.cattod.2007.06.005

conditions of catalysts, to investigate the mechanism of SMSI in oxidative atmosphere is of great necessity.

In this work, two series of Pt-supported CeO_2–ZrO_2–La_2O_3 (CZL) samples were prepared: one was received by impregnating Pt on CZL calcined upon different temperatures and then calcined at the same temperature, the other was obtained by calcining the same impregnated CZL at different temperatures. XRD, BET, XPS, FTIR, HRTEM and catalytic activity evaluation are performed to investigate the influence of SMSI on the thermodynamic performance of metal and CZL support. Also, the effect of SMSI on the structural and chemical properties of catalysts after oxidative calcinations is studied.

2. Experimental

2.1. Catalysts preparation

CeO_2–ZrO_2–La_2O_3 (CZL) mixed oxides were synthesized by citric-aided sol–gel method. The nitrates $Ce(NO_3)_3{\cdot}6H_2O$, $ZrO(NO_3)_2{\cdot}5H_2O$ and $La(NO_3)_3{\cdot}6H_2O$ were mixed according to the molar ratio of Ce:Zr = 67:33 and weight content of La^{3+} = 2%. Citric acid was used as the complexing agent. Appropriate glycol was added as the dispersant followed by evaporation and peptization. The sol was heated at 100 °C until a spongy yellow gel remained. Then the gel was divided into three shares and submitted to decomposition at 300 °C for 1 h and calcinations at 500, 700 and 900 °C in static air for 3 h, respectively. A portion of the CZL powders calcined at 500 °C was further aged at 1050 °C in static air for 6 h to obtain stabilized surface and phase properties. These as-prepared powders were named after the calcination temperatures and hereafter referred to as C5, C7, C9 and CK, respectively.

Pt was loaded on C5, C7, C9 and CK by impregnating these powders in the aqueous solution of H_2PtCl_6. The nominal weight content of Pt is 2%. The impregnated C5, C5 and C7 were calcined at 500 °C in static air for 3 h to obtain so-called P5C5, P5C7 and P5C9, respectively. Meanwhile, the impregnated CK was divided into three shares and thermally treated at 500, 700 and 900 °C in static air for 3 h to gain P5CK, P7CK and P9CK, respectively. The series of P5C5, P5C7, P5C9 and P5CK was hereafter called P5 samples while the series of P5CK, P7CK and P9CK was called CK samples for short.

2.2. XRD diffraction

The powder X-ray diffraction (XRD) experiments were performed on a Japan Science D/max-RB diffractometer employing Cu Kα radiation (λ = 1.5418 Å). The X-ray tube was operated at 40 kV and 120 mA. The X-ray powder diffractogram was recorded at 0.01° intervals in the range of $20^\circ \leq 2\theta \leq 80^\circ$ with scanning velocity of $2^\circ\,min^{-1}$. The identification of the phase was made with the help of the JCPDS cards (Joint Committee on Powder Diffraction Standards). The crystallite sizes and lattice constants of CZL were determined using the software XRDTHX.

2.3. BET surface area

The specific surface area was determined by Brunauer–Emmett–Teller (BET) method with a Quantachrome NOVA instrument using Ar as carrier and N_2 as adsorbent.

2.4. XPS

The X-ray photoelectron spectroscopy (XPS) experiments were carried out on a PHI-Quantera SXM system equipped with a monochromatic Al Kα X-rays under UHV (6.7×10^{-8} Pa). A 100 μm spot size was used for analysis. Sample charging during the measurement was compensated by an electron flood gun. The electron takeoff angle was 45° with respect to the sample surface. The XPS data from the regions related to the C 1s, O 1s, Zr 3d, La 3d, Ce 3d and Pt 4f core levels were recorded for each sample. The binding energies were calibrated internally by the carbon deposit C 1s binding energy (BE) at 284.8 eV. A linear background was used for the fitting of peaks with the program XPSPEAK 4.0.

2.5. CO chemisorption followed by FTIR spectroscopy

For the IR studies, the samples were pressed into disks, respectively. In order to avoid the impacts induced by impurities on the surface, all samples were pretreated according to the procedure described as follows: the disks were heated from room temperature to 200 °C at 20 °C min^{-1} in air and reduced in H_2 at that temperature for 2 h, then the reduction was followed by an evacuation at 200 °C for 3 h. After being cooled down to room temperature in vacuum, each disk was submitted to the in situ CO adsorption. Small doses of CO were introduced to the wafer and the spectra were recorded by Nicolet Magna 760 FTIR spectrometer and processed using the Nicolet OMNA software.

2.6. HRTEM

High resolution transmission micrographs were shot by a JEOL 2011 electron microscopy, operating at 200 kV with a point-to-point resolution of 0.18 nm. Before the observations, the powder samples were diluted in the ethanol and dispersed by ultrasonic. Afterward, a drop of each solution was deposited on a Cu grid coated by a holed carbon film and dried in air. The crystal plane distances were measured directly on these micrographs and compared with JCPDS cards of the species possibly present in the chemical system considered.

2.7. Activity measurement

The powder catalyst sample was weighed for 0.5 g and mixed homogeneously with appropriate volume of coarse quartz particles to 3 ml. The mixture was loaded in a quartz reaction tube with the diameter of 25 mm. The three-way catalytic activity was evaluated in a tube micro-reactor by passing a gas mixture simulated to exhaust from gasoline engine. The simulated exhaust contained a mixture of O_2

(1.5%), CO (1.5%), H_2 (0.5%), CO_2 (12%), C_3H_8 (0.1%), NO (0.05%) and N_2 (balance), corresponded to an oxidants/reductants stoichiometric factor $S = (2O_2 + NO)/(CO + 10C_3H_8)$ of 1.2. The concentrations of CO, C_3H_8 and NO were determined on-line by a five-component analyzer FGA4015 with infrared sensor. For the light-off experiments, the reactor was heated from 150 to 550 °C in the flow stream at a gas space velocity of 50,000 h^{-1}.

3. Results and discussion

3.1. Structural and textural properties

Table 1 summarized the structural and textural properties of CZL and Pt-supported samples. According to the data of S_{BET} and d_{CZL}, thermal treatments at different temperatures obviously induce distinct sintering of CZL. It is seen that the ageing treatment at 1050 °C for 6 h is severe enough to raze the porous surfaces of CZL to smooth ones and to drive the growth of crystallites.

Fig. 1a shows the XRD patterns of CZL treated at different temperatures. The main peaks of XRD patterns of all the samples are consistent with the characteristic peaks of cubic CeO_2 while presenting superiority in symmetry, which confirms the formation of CeO_2–ZrO_2–La_2O_3 solid solutions. The main peaks experience a sharpening as the calcination temperature increases from 500 to 1050 °C, which indicates the growth and integrity of crystal grain. XRD patterns of the Pt-supported CZL are shown in Fig. 1b. Besides the main peaks of CZL, the characteristic peaks of metallic Pt are observed for all the samples except P5C5. The sequences of P5C7 < P5C9 < P5CK and P9CK < P7CK < P5CK are observed when looking at the peak intensity of Pt (1 1 1). The former sequence implies the integrity of Pt crystalline associated with the sintering of metal particles. This can be easily explained by the surface density of Pt, an indicator introduced to help describe the theoretical weight content of Pt per unit area of the support, supposing all Pt atoms are homogeneously dispersed on the surface. It is seen from the values of surface density of Pt in Table 1 that impregnation of Pt on supports with different surface areas may lead to distinguishable distributions of Pt particles on the supports. During calcinations, metal atoms have more statistical probability to encounter with each other when dispersed on a surface of lower surface area, which brings about the facility to form larger Pt crystallites. In addition, no Pt species are detected for P5C5, which might be attributed to the well-dispersion of fine Pt particles on the high-surface area support. However, the latter sequence seems to be conflictive with the

Table 1
Structural and textural properties of CeO_2–ZrO_2–La_2O_3 mixed oxides and the Pt-supported samples

Samples	S_{BET} ($m^2\ g^{-1}$)	d_{CZL}[a] (Å)	a[b] (Å)	Surface density of Pt[c] ($g\ m^{-2}$)
C5	81.8	59	5.347 ± 0.001	–
C7	31.5	61	5.352 ± 0.001	–
C9	5.9	126	5.345 ± 0.001	–
CK	4.3	187	5.343 ± 0.001	–
P5C5	55.6	64	5.337 ± 0.001	3.60×10^{-4}
P5C7	12.5	63	5.341 ± 0.001	1.60×10^{-3}
P5C9	6.6	131	5.342 ± 0.001	3.03×10^{-3}
P5CK	4.2	197	5.340 ± 0.001	4.76×10^{-3}
P7CK	5.5	197	5.347 ± 0.001	3.64×10^{-3}
P9CK	5.3	201	5.345 ± 0.001	3.77×10^{-3}

[a] Average diameter of crystallite of CZL mixed oxides determined from XRD peak of (2 2 0) crystal plane using the program XRDTHX.
[b] Mean lattice constant calculated based on XRD peak of (2 2 0) crystal plane using the program XRDTHX.
[c] A theoretic value calculated by the ratio of 2 wt.%(Pt)/S_{BET}(catalyst), supposing Pt atoms are all distributed homogeneously on the surface of supports.

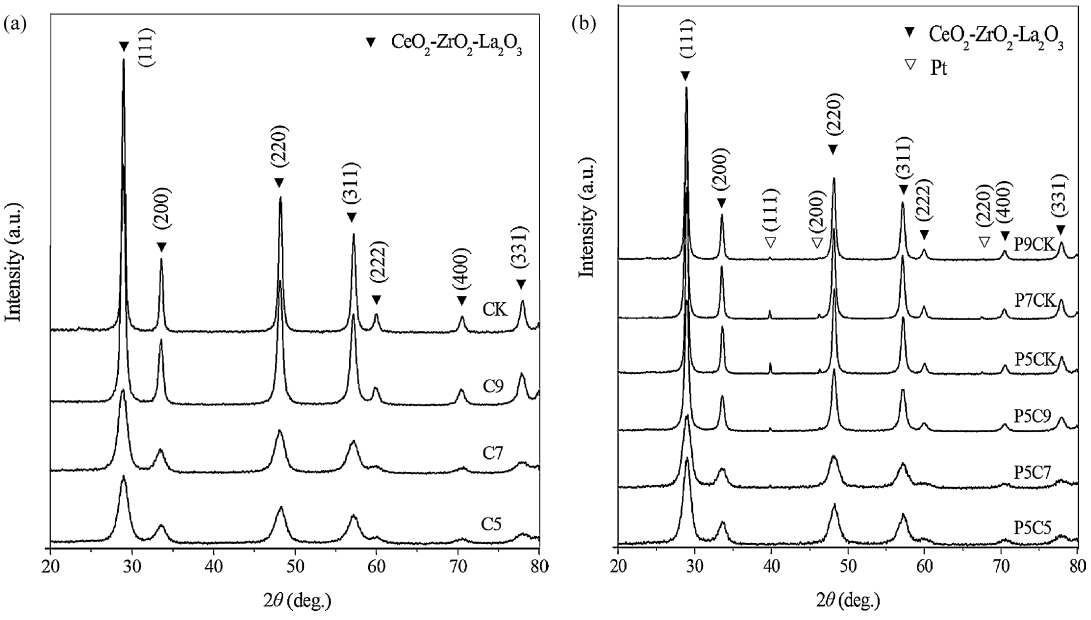

Fig. 1. XRD patterns of the CeO_2–ZrO_2–La_2O_3 mixed oxides (a) and the Pt-supported samples (b).

normal understanding that Pt would suffer more severe sintering at higher temperatures and accordingly present sharp diffraction peaks. One possible reason for this can be elucidated as an inward diffusion of Pt or an outward diffusion of support leading to the encapsulation of the metal by the support, which weakens the received signals of the diffractive X-ray.

Zr^{4+} and La^{3+} ions are considered to have been inserted into the lattice of ceria since the formation of CZL has been confirmed. In respect that the radii of Zr^{4+} and La^{3+} ions are 0.84 Å and 1.18 Å, respectively, the content of Zr^{4+} and La^{3+} in the bulk of ceria reflects on the change of the lattice constants d, which were calculated based on Bragg's Law $2d \sin\theta = k\lambda$ and the crystal plane of (2 2 0) as the reference plane. Meanwhile, Ce^{3+} ions (1.14 Å for eight-coordination) is larger than Ce^{4+} (0.97 Å) suggesting that the conversion between Ce^{3+} and Ce^{4+} affects the mean lattice constants. In addition, it is observed from Table 1 that compared with corresponding supports, the samples of P5C5, P5C7, P5C9 and P5CK show a contraction of the crystal cell whereas P7CK and P9CK show expanded lattices, which indicates the influence of metal on the lattice structures. The effect of inserted metal ions on the lattice size of the support could not be neglected as long as the SMSI is being considered and discussed. For the Pt-supported samples, the variation of lattice constants depends on the synergistic effect of substitution between Ce^{4+} and doped ions, conversion of Ce^{4+}/Ce^{3+} and structural re-organization induced by metals.

3.2. XPS analysis

An XPS investigation was conducted to explore the distribution of the elements on the surface and the variations of the oxidation states of cerium and platinum.

The surface elemental compositions of the metal supported samples calculated from the normalized peak areas of the Ce 3d, Zr 3d, La 3d, Pt 4f and O 1s core level spectra are shown in Table 2. The Ce/Zr atomic ratios of all the samples, especially P5C7 and P9CK, are lower than the theoretic value of 2.0, indicating an enrichment of Zr species at the periphery of the particles, i.e. a shell/core structure. It can be deduced from the comparison between the surface La content of P5C5, P5C7, P5C9 and P5CK that an outward diffusion of La from the bulk to the surface of the particles occurs as the supports are calcined at increasing temperatures. The similar observation was reported by Kašpar et al. [4], who believed that the ceria crystallite growth under oxidizing conditions could be impeded by the tri-valent enrichment.

Moreover, for the P5 samples, the surface content of Pt increases with the dwindling in surface areas of the supports. It can be mainly ascribed to the high surface density of Pt on the low-surface area support in the case that the impregnated metal is of the same weight content for different samples. Take P5CK as an example, though the metal particles supported by CK maintain lower dispersion because of more severe sintering of metal, the extremely high Pt concentration (about 10 times as high as that of P5C5) reflects on the high surface content of Pt derived by XPS. Considering the loss of surface areas of C5 and C7 during the process of impregnation and the sequent calcinations, another possible reason for the much lower Pt surface contents of P5C5 and P5C7 is that the calcinations for the decomposition of H_2PtCl_6 destruct the porous supports to some extent and encapsulate the Pt particles in the supports. Thus, the low-surface area powders possessing fewer micropores could support more exposed metals while presenting unsatisfying efficiency in retarding the sintering of metals.

Moreover, it is observed from the XPS results that, for the CK samples, the thermal treatments at higher temperatures for the decomposition of H_2PtCl_6 lead to an evident loss of surface Pt while the XRD patterns present weakened peak intensities of Pt. For P9CK even hardly could any signals of Pt species be detected by XPS whereas XRD technique is able to detect the weak peaks of Pt as show in Fig. 1b, suggesting the existence of Pt in P9CK. This phenomenon may be attributed to the complete encapsulation of Pt particles by ceria species at high temperature. Since the detection depth of XRD extends to more interior sphere of the particles than that of XPS, the signals collected by these two characterization techniques actually carry the information of different atom layers. Therefore, the XRD pattern indicates the existence of Pt enveloped in the bulk of support while XPS implies the absence of Pt species on the surface.

In order to obtain more information of oxidation states of the surface elements, the O 1s, Ce 3d, and Pt 4f XPS spectra were analyzed, respectively.

The spectra for the O 1s ionization feature are numerically fitted with two Gaussian–Lorenz features, which are shown in Fig. 2. The primary band (529.4–529.7 eV) denoted as O_{latt}

Table 2
Surface elemental composition and atomic ratio of the Pt-supported samples measured by XPS

Sample	Surface composition (at.%)						Ce/Zr	$O_{latt}/Ce + Zr + 1.33La + 2Pt$[a]
	Ce 3d	Zr 3d	La 3d	Pt 4f	O 1s			
					O_{ads}	O_{latt}		
P5C5	12.57	10.49	0.49	0.75	18.43	57.28	1.20	2.27
P5C7	8.65	8.47	0.39	0.64	48.26	33.58	1.02	1.78
P5C9	10.97	8.89	0.91	2.00	32.78	44.45	1.23	1.77
P5CK	8.39	6.66	1.88	3.09	45.52	34.46	1.26	1.45
P7CK	11.64	9.12	1.17	0.50	21.17	56.39	1.28	2.42
P9CK	9.64	9.94	1.67	0	27.46	51.29	0.97	2.35

[a] Assuming that La and Pt species present in the form of La_2O_3 and PtO, respectively.

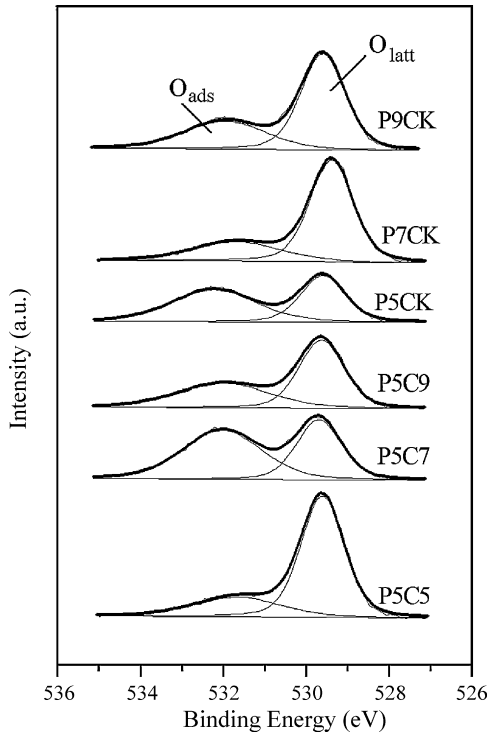

Fig. 2. O 1s spectra for the Pt-supported CeO_2–ZrO_2–La_2O_3 mixed oxides.

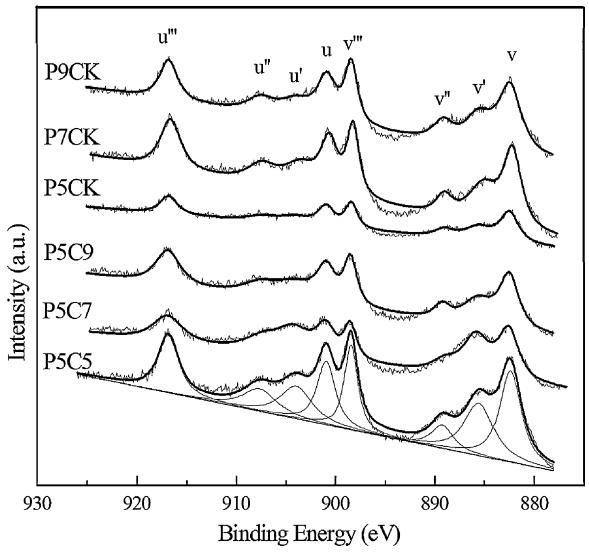

Fig. 3. Ce 3d spectra for the Pt-supported CeO_2–ZrO_2–La_2O_3 mixed oxides.

represents the O 1s ionization for oxygen associated with the ceria–zirconia–lanthana mixed oxides, while the additional band (531.6–532.2 eV) denoted as O_{ads} is the result of adsorbed molecular oxygen, water or –OH species [13]. The relative percentages of these two oxygen species are quantified based on the area ratios of O_{latt} and O_{ads} peaks. According to the calculations of multiplying the relative percentages by the corresponding surface elemental content of O 1s, the surface atomic contents of O_{latt} and O_{ads} species for the Pt-supported samples are determined and the results are listed in Table 2. Since O_{latt} is considered as the intrinsic constituent originating from the electrovalent bonding with Ce, Zr and Pt ions, the atomic ratios concerning O_{latt} are introduced to characterize the stoichiometry of the surface, and the mentioned atomic ratios are listed in Table 2 as well.

As listed in Table 2, the ratio of $O_{latt}/Ce + Zr + 1.33La + 2Pt$ exposes the nonstoichiometry of the Pt-supported samples indirectly assuming that O^{2-} ions coordinate with Ce^{4+}, Zr^{4+}, La^{3+} and Pt^{2+} forming stoichiometric compounds. The experimental ratios are not precise enough to be compared exactly with the theoretical value 2.0, however, the catalysts may be classified in descending order of P9CK > P7CK > P5C5 > P5C7 ≈ P5C9 > P5CK. These values are mainly determined by three factors: (i) the existence of Ce^{3+}, (ii) oxygen vacancies and (iii) extra oxygen species. The last factor arises from carbon bonding with the binding energy of 534.9–542.6 eV [14] and increases the ratios. On the other hand, a lot of oxygen vacancies are created by the doping of tri-valent La according to Cho [15], reduction of Ce^{4+} to Ce^{3+} and lattice distortion by doping of Zr^{4+}, which favors the decrease of the ratios. The existence of oxygen vacancies can promote the chemisorption of oxygen from gas and make them activated by a series of oxygen transfer between the surface and bulk.

As shown in Fig. 3, the curves of Ce 3d spectra are fitted with eight peaks corresponding to four pairs of spin–orbit doublets. The labeling of the peaks follows the convention. Letters *u* and *v* refer to the $3d_{3/2}$ and $3d_{5/2}$ spin–obit components, respectively. The spin–orbit splitting is 18.4 eV in accordance with the literature [13,14,16,17]. The peaks marked as *u* (900.6–901.0 eV), *u″* (907.5–907.7 eV) and *u‴* (916.6–916.9 eV) arise from Ce^{4+} $3d_{3/2}$ while the peaks labeled as *v* (882.2–882.6 eV), *v″* (889.1–889.3 eV) and *v‴* (898.2–898.5 eV) arise from Ce^{4+} $3d_{5/2}$. The couple corresponding to one of the two possible electron configuration of the final state of the Ce^{3+} species are labeled as *u′* (903.5–904.2 eV) and *v′* (885.1–885.8 eV). Meanwhile, the Pt 4f spectra of all the samples are shown in Fig. 4. The peaks located at 72.6–72.9 eV are attributed to Pt^{2+} $4f_{7/2}$ while the peaks at 70.7–70.9 eV are assigned to Pt^0 $4f_{7/2}$. The binding energies of 72.8 eV and 70.9 eV held by P5C5 and P5C7, respectively, are marked in Fig. 3 as reference values of Pt^{2+} $4f_{7/2}$ and Pt^0 $4f_{7/2}$. A spin–orbit splitting of 3.35 eV according with the literature [18] was fixed as constraint in the fitting procedure of peak positions. The relative percentages of the cerium species and platinum species are obtained by the area ratios of the Ce^{4+} $3d_{5/2}$ (*v*, *v″* and *v‴*)/Ce^{3+} $3d_{5/2}$ (*v′*) and Pt^{2+} $4f_{7/2}$/Pt^0 $4f_{7/2}$, respectively. The surface contents of these species are obtained according to the calculations of multiplying the relative percentages by corresponding surface elemental content, and the results are listed in Table 3.

As shown in Table 3, the differences between the surface contents of Ce^{3+} are neglectable for all samples although the Ce^{3+} percentage in ceria varies from each other. Thus, combining with the discussion above, we are convinced that in this work it is not the abundance of Ce^{3+} but the oxygen vacancies that plays one of the essential roles in the catalytic performances.

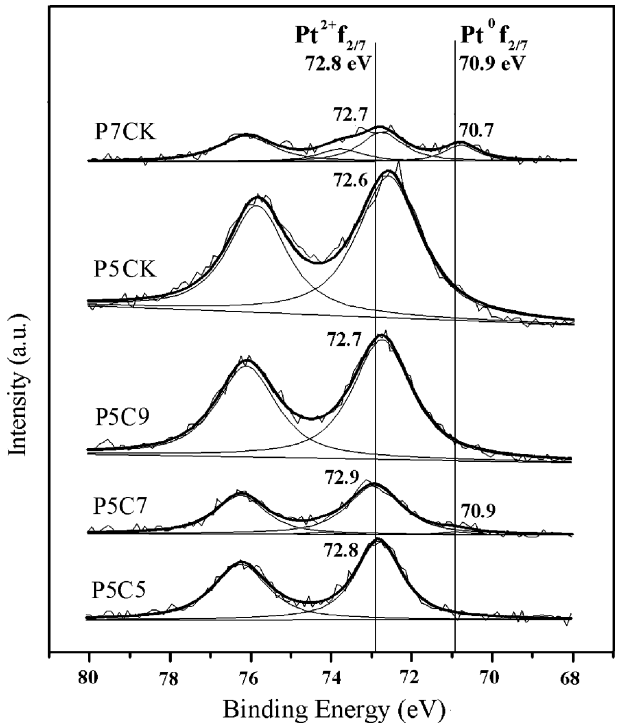

Fig. 4. Pt 4f spectra for the Pt-supported CeO_2–ZrO_2–La_2O_3 mixed oxides.

As can be seen from Fig. 4 and Table 3, platinum almost presents as platinum oxide of the PtO type for the P5 samples, which seems to be inconsistent with the XRD patterns claiming the presence of Pt metal instead of PtO. According to the above paragraphs, the distinguishable detection depths of XRD and XPS give a conceivable explanation. Based on our former research [19], it is believed that the Pt particles are actually enveloped by compact platinum oxide layers, which are more easily influenced by surroundings including the support and atmosphere.

As shown in Fig. 4, the peak intensities of Pt 4f spectra are in accordance with the surface elemental content of Pt species. Moreover, it is observed that the peak positions of Pt^{2+} $4f_{7/2}$ shift towards lower binding energies by about 0.3 eV for P5C9, P5CK and P7CK. According to literatures, this decrease can be explained by metal particle growth [17,20]. For the samples with high dispersion of platinum, the electrons emitted from platinum atoms would not be affected by the shadowing effect of the neighboring atoms. However, the shadowing becomes more important with the growth of particles resulting in the decrease of binding energy, which even reaches the bulk metal value. The binding energy of well-dispersed platinum is reported to be approximately 0.5 eV larger than the bulk metal value [20]. As reported by many research groups [7,9], PtO in P7CK experiences a decomposition during the high temperature calcination. Similarly, the as-received Pt metals suffer a severe sintering since a lower binding energy of Pt^0 $4f_{7/2}$ is evident compared with the reference value processed by P5C7. This result agrees well with the XRD patterns which assures the sintering of Pt particles during the calcinations following the impregnation for P5C9, P5CK and P7CK.

Table 3
Oxidation state and surface composition of the Ce and Pt species derived from XPS analyses

Sample	Ce^{4+} $3d_{5/2}$ (at.%)		Ce^{3+} $3d_{5/2}$ (at.%)		Pt $4f_{7/2}$ (at.%)	
	In Ce	On surface	In Ce	On surface	Pt^0 in Pt	Pt^{2+} in Pt
P5C5	70.3	8.8	29.7	3.7	0.0	100.0
P5C7	60.0	5.2	40.0	3.5	4.5	95.5
P5C9	70.2	7.7	29.8	3.3	0.0	100.0
P5CK	73.2	6.1	26.8	2.2	0.0	100.0
P7CK	69.8	8.1	30.2	3.5	17.0	83.0
P9CK	76.1	7.3	23.9	2.3	–	–

3.3. CO adsorption

To obtain more detailed information about the influence of CZL supports on the properties of Pt, such as dispersion and chemisorption ability of Pt, CO adsorption was performed followed by FTIR spectroscopy. The IR spectra corresponding to chemisorbed CO on P5C5, P5C7, P5C9 and P9CK are shown in Fig. 5. The spectra for P5CK and P7CK are not reported here since no chemisorbed CO species are detected.

Obviously, P5C5, P5C7 and P5C9 show typical spectra of CO adsorbed on Pt. Different adsorption sites can be assessed on the catalysts by the analyzing of the ν(CO) bands. The bands at 2075 cm^{-1} are ascribed to the linearly adsorbed CO species (L) on Pt crystallites [21], while the bands located at wavenumbers below 1900 cm^{-1} are due to multi-bound CO species, i.e. a doubly bridged (B) species at 1843 cm^{-1} and a 3FC species at 1800 cm^{-1}. The carbonate formation gives rise to the bands at ca. 1602 cm^{-1}. Perrichon et al. [22] have proved that the measurement of platinum dispersion by CO adsorption at room temperature followed by IR spectroscopy is a reliable method, as that using H_2 chemisorption at −78 °C after reduction at 200 °C. Since the percentages of B CO species and 3FC CO species are relatively much lower, the adsorption

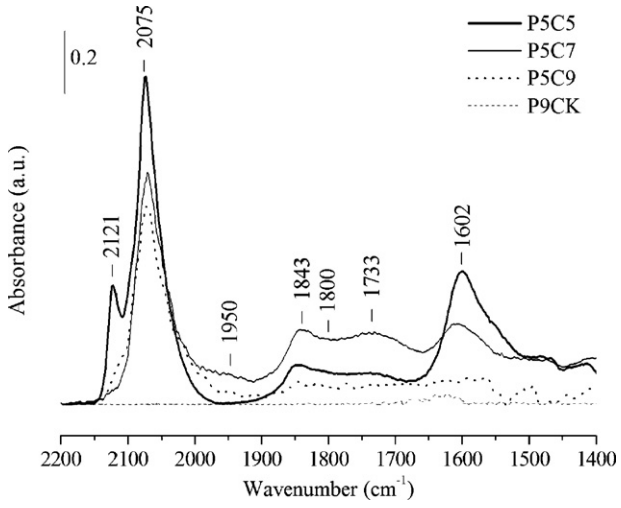

Fig. 5. FTIR spectra of CO adsorption over the Pt-supported samples at room temperature, after reduction at 200 °C.

Table 4
Platinum dispersion measured by CO chemisorption using FTIR

Samples	Integrated intensity (cm^{-1})	Adsorbed CO[a] (μmol)	D (%)	d_{Pt} (nm)	S_{Pt} ($m^2\ g^{-1}$)
P5C5	11.568	0.418	40.8	2.7	103.6
P5C7	8.601	0.259	25.3	4.3	65.1
P5C9	8.148	0.254	24.8	4.4	63.6

[a] Obtained by applying the functional relationship between the integrated intensity of the ν(CO) bands for platinum and the CO doses introduced in Ref. [22].

stoichiometry CO/Pt can be figured as 1. The amount of surface platinum sites (Pt_{surf}) hereby can be easily calculated (equal to the number of adsorbed CO at metal saturation) and then the Pt dispersion (D) can be obtained by the ratio Pt_{surf}/Pt_{total}, where Pt_{total} is calculated by the loading content of 2 wt.%. The average diameter of Pt crystallites (d_{Pt}) is obtained by d_{Pt} (nm) = 1.1/D as reported in literature [23], and the surface area of Pt particles is estimated by using the formula S_{Pt} ($m^2\ g^{-1}$) = 6000/(ρd_{Pt}) [24], where ρ stands for the density of Pt metal. Thus, the CO adsorption provides us with some structural and textural properties that cannot be derived from XRD or XPS. The results are reported in Table 4. Actually, both the values of D and S_{Pt} rely on those of d_{Pt}, which change with metal sintering. Again, more severe sintering of Pt for P5C7 and P5C9, which has been observed by XRD and XPS, is confirmed.

In Fig. 5, the shoulders at ca. 2121 cm^{-1}, especially visible for P5C5, are attributed to the CO species adsorbed on Pt^{2+}, while the ones at ca. 1950 cm^{-1} and 1733 cm^{-1} are due to CO coordinated to both Pt and Ce [22]. There is no denying that the varieties of these shoulders indicate the different states of Pt adsorption sites and Pt/Ce interface, e.g. the abundance of chemisorption sites on the Pt/Ce interface of P5C7.

It is surprising that the CK samples show no detectable bands except for the ones at ca. 1630 cm^{-1} for P9CK although XPS assures the existence of Pt on the surface for P5CK and P7CK. Since the adsorption of CO were carried out at room temperature, which allow us to rule out the oxidation of CO during the recording of the IR spectra, the zero-adsorptions for the CK samples are attributed to their intrinsic characteristics. The disappearance of chemisorption sites may be due to the following reasons: (i) the sintering of metal particles, which leads to the decrease of surface platinum atoms; (ii) the SMSI occurred in oxidative calcinations of the samples. For P7CK and P9CK, the XRD and XPS analyses have brought forward the possible mechanism that partial Pt particles are enveloped by CZL support during the high-temperature calcination for the decomposition of H_2PtCl_6. Here, the loss of chemisorption sites promotes the reliability of the mentioned mechanism since the Pt crystallites covered by support hardly adsorb any CO; (iii) the occupation of adsorption sites by H atoms introduced in the pretreatment. Usually, adsorption is described in terms of the probability that molecules impinging on a surface adsorb instead of scatter back into the gas phase. The sticking probability changes significantly with coverage, primarily because of the filling up of adsorption sites on the surface [25]. Gland et al. [26] reported that coadsorbed H_2 could weaken the adsorption of CO on Pt (1 1 1). In this work, the larger metal particles of CK samples have already lead to the decrease of surface sites. As revealed in the following section concerning the TWC activities, the oxygen species on CK samples are less active than those on P5C5, P5C7 and P5C9 at 200 °C. Therefore, the residual H atoms adsorbed on CK samples may be more than those on P5 samples (without P5CK) after pretreatment and hereby brings about an obviously weakened adsorption of CO. However, the reasons mentioned above are

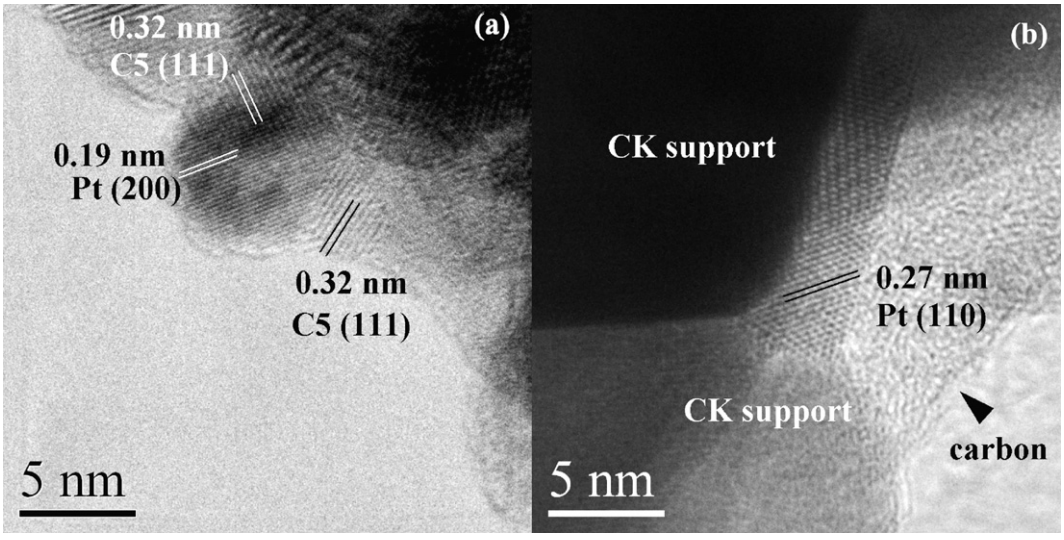

Fig. 6. HRTEM micrographs of P5C5 (a) and P9CK (b).

still not satisfying enough to explain the absence of Pt sites for CK samples. Other possible mechanisms, which lead to the complete deactivation of chemisorption sites of Pt, including the sites on the Pt/Ce interface, still remain to be investigated.

3.4. HRTEM

The surface Pt contents of P5C5 and P9CK are lower than that of P5CK. The former is mainly attributed to the low surface density of Pt and possible encapsulation by support during the decomposition of H_2PtCl_6 while the latter is supposed to be explained by encapsulation mechanism on the basis of XRD, XPS and FTIR analysis. High resolution transmission electron microscopy is applied to investigate more detailed information about the microstructures of P5C5 and P9CK in order to submit evidence for the hypothesis.

As shown in Fig. 6a, it is obvious that the metal particle is partially enveloped by C5 support although the sample has not experienced any reductive pretreatment. This observation strongly supports the explanation of encapsulation mechanism in oxidative atmosphere. In Fig. 6b, the sintering of the CZL particles is observed for P9CK. The observed metal particle is not only located on the surface of the support but also surrounded by the support particles. Hence, the number of surface metal atoms exposed to the detection of XPS is much smaller than that of Pt well-dispersed samples, which directly leads to weakened signals. Also, this type of surrounding or encapsulation by the support is considered to be one of the possible reasons for the loss of chemisorption sites of Pt.

3.5. Catalytic performances

The catalytic activities of Pt-supported samples were evaluated and the light-off curves of C_3H_8, CO and NO are shown in Fig. 7. It is very obvious that the performances for these Pt-supported samples in converting different pollutants follow the same sequence of P5C9 > P5C7 > P5C5 > P5CK > P7CK > P9CK. P5C9 performs only slightly better than P5C7 while both of them are evidently superior to the others.

In view of the effect of ceria–zirconia–lanthana mixed oxides, the catalytic activities of Pt-supported samples are significantly influenced by the concentration of oxygen vacancies. Tschöpe et al. [27] concluded the importance of nonstoichiometry by investigating the oxidative activities of La and Cu-doped CeO_{2-x}. Also, Rao et al. [28] figured that the bulk oxygen vacancies played an important role in promoting NO conversion over Pt- and Rh-loaded CeO_2–ZrO_2 catalysts. Moreover, Bozo et al. [11] pointed that the presence of a small amount of oxygen vacancies could strongly improve the catalytic activity of $Pt/Ce_{0.67}Zr_{0.33}O_2$. They summarized the key roles of oxygen vacancies on catalytic activities as (i) promoting the oxygen activation and mobility in the support and (ii) allowing the presence of quasi-free electrons, which contributed to the electronic enrichment of the noble metal. In the case that the surface Pt species of P5C5 and P5C7 are almost in the similar content and sintering state, the unsatisfying activity for P5C5 can be mainly attributed to the lack of oxygen defects as discussed in the XPS part. Similarly, the low activities of P7CK and P9CK can be partially ascribed to this reason.

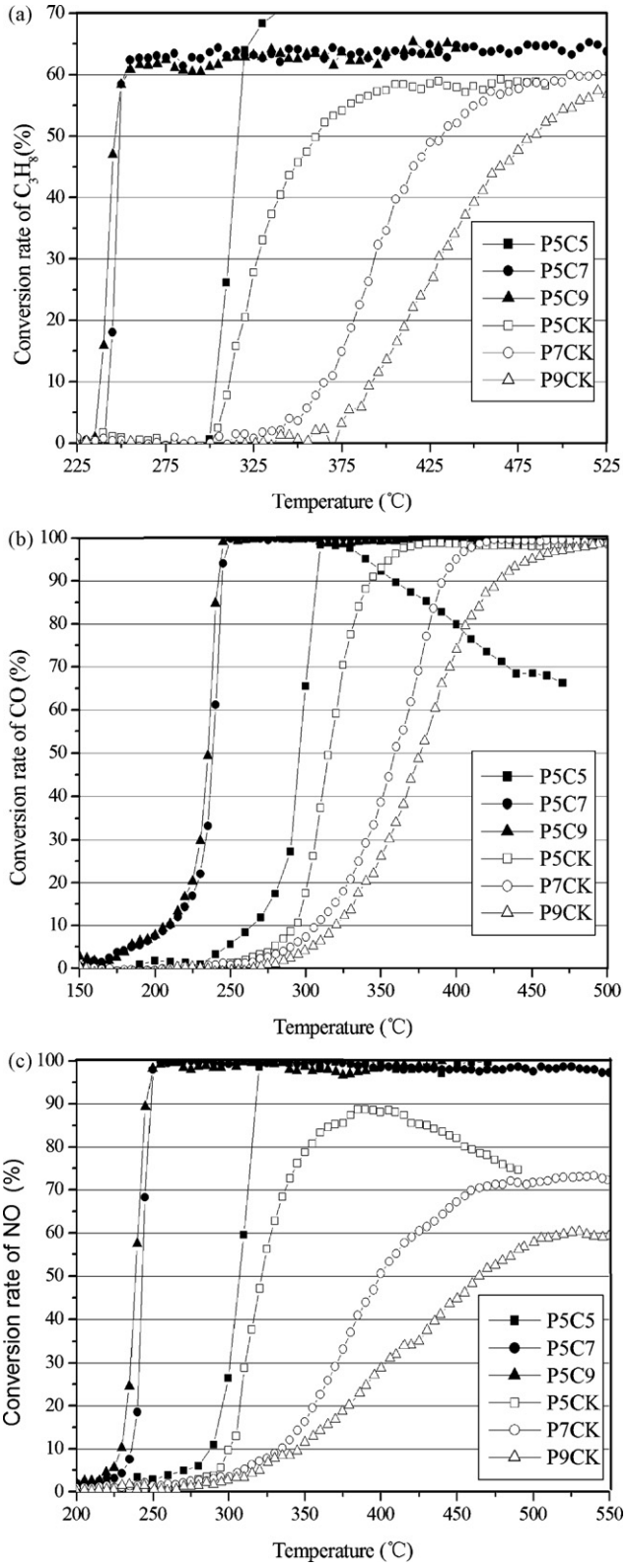

Fig. 7. Light-off curves of the C_3H_8 (a), CO (b) and NO (c) for the Pt-supported CeO_2–ZrO_2–La_2O_3 mixed oxides.

On the other hand, the participation of Pt is responsible for the catalytic activities. As suggested by Passos et al. [29], metal–support interfacial area contributed to the performance on partial oxidation of methane, and the increase of metal particle size decreased the metal–support interfacial area, which could explain the deactivation of catalyst during the reaction. Moreover, according to Golunski et al. [30] and our former work [19], the activities for HC and NO rely heavily on the chemisorption of Pt, which focuses on the Pt^0 sites, while the interaction of CO depends on the Pt^0 sites, the interfacial Pt sites and the ceria in the vicinity of Pt particles. In this work, the XPS results discussed above indicate that the Pt^0 sites are almost covered by platinum oxide layers for the as-prepared Pt-supported samples. However, the strongly adsorbed linear CO species on PtO surface [21] and the headmost conversion of CO among the pollutants, which result in the reduction of PtO with the formation of CO_2, allowing us to emphasize the role of Pt^0 sites on the three-way catalytic activities. As a matter of fact, the sintering process, which congregates many tiny particles and fuses into a larger one, rises serious loss of both the metal–support interfacial area and the active sites, since metal dispersion values decrease steeply when the particles grow up in the size range of 0–8 nm [6]. Therefore, it is not the surface Pt content but the appropriate metal particle size that makes contribution to the enhancement of catalytic activities. In this work, for P5CK, P7CK and P9CK, the lack of chemisorption sites of Pt, which is due to the severe sintering and the encapsulation of Pt aggravates the deterioration of the catalytic activities. In the case of P5C5, P5C7 and P5C9, the light-off curves imply that it is not the smallest particle with the highest dispersion results in the best catalytic activities. This may indicate that it is the integrated crystal phase of Pt rather than the atomic cluster that is more contributive to the promotion of catalytic activities.

Moreover, the possible effect of enriched surface La species on catalytic performances cannot be neglected. As mentioned by Frost [31], the metal promotes the oxide by enhancing the equilibrium concentration of oxygen vacancies: electron transfer from the oxide to the noble metal results in a lowering of the effective activation energy for the formation of oxygen vacancies. This actually emphasizes the important effect of the electron transfer between support and Pt on the catalytic performances. Kharlanov and co-workers [32] observed that the introduction of tri-valent Y^{3+} or La^{3+} cations to CeO_2–ZrO_2 mixed oxides reduced the amount of electron-acceptor sites belonging to cerium cations, stabilizing ones as Ce^{3+}. Hereby, the possible linkage of La between Pt and support should be paid more attention to. According to the preparation procedure for the CK samples, Pt was impregnated on calcined CK powders with enriched La species. Thus, it is probable that the La species are sandwiched between Pt and support particles. The question that whether an electron-block or an electron-transmit effect is available during interactions needs further investigations.

In addition, P5C5 shows higher conversion rate than the other catalysts when the temperature increases above 320 °C. To explain this phenomenon, the fact that the CO conversion over P5C5 decreases simultaneously should be taken into account. It seems that there is a competitive adsorption of CO and C_3H_8 on Pt active sites. Considering the dispersion of Pt particle, we conjecture that smaller metal particles seem to be more selective for the adsorption of C_3H_8 while CO is more competent for the adsorption on larger metal particles.

4. Conclusions

The CeO_2–ZrO_2–La_2O_3 supports with different surface areas present significant influence on the distribution of Pt on the surface of the supports. XRD patterns, XPS analysis and FTIR spectra show that for P5 samples, the high-surface area supports present the ability to retard the agglomeration and sintering of Pt by possessing much lower surface Pt densities. The low surface content of Pt for P5C5 is partially ascribed to the encapsulation of Pt by Ce species, which is considered to be induced by the collapse of porous structure of the high-surface area support.

The encapsulation phenomenon is also investigated from the angle of CK samples by calcinating the Pt-loaded low-surface area supports at different temperatures. It is found that the higher the calcination temperature is, the less the surface content of Pt is. Especially, P9CK even exhibits the disappearance of detected signals of surface Pt species, which also suggests the occurrence of encapsulation. However, different from the case of P5C5, the encapsulation mechanism for P9CK is considered to originate from the inward diffusion of Pt or outward diffusion of support. Although the encapsulation phenomenon acting as an important mechanism of the SMSI is observed mainly after reductive treatment at high temperature, the XPS, XRD, CO adsorption and HRTEM analyses in this work raise its possible occurrence in oxidative atmosphere.

The light-off curves figure the catalytic performances of the Pt-supported sample in the sequence of P5C9 > P5C7 > P5C5 > P5CK > P7CK > P9CK. Compared with that of P5C5, the outstanding activities of P5C9 and P5C7 are mainly attributed to the chemisorption sites of Pt and abundant oxygen vacancies. Beside the negative effect of lacking of oxygen defects, another reason for the progressively deteriorated activities of Pt-supported CK samples is the sintering and the encapsulation of Pt particles, which leads to the decrease of chemisorption sites on the metal surface and interfacial area. The effect on catalytic activities induced by the enrichment of La is calling for further investigations.

Acknowledgements

The authors would like to acknowledge the Ministry of Science and Technology, PR China for the financial support of Project 2004CB719503 and National Natural Science Foundation of China for the financial support of Project 50502023. Moreover, we would also thank the Center of Analysis and Key Lab of Advanced Materials in Tsinghua University.

References

[1] M. Ozawa, J. Alloys Compd. 275–277 (1998) 886.
[2] T. Masui, T. Ozaki, K. Machida, G. Adachi, J. Alloys Compd. 303/304 (2000) 49.
[3] K. Kenevey, F. Valdivieso, M. Soustelle, M. Pijolat, Appl. Catal. B: Environ. 29 (2001) 93.
[4] J. Kašpar, P. Fornasiero, M. Graziani, Catal. Today 50 (1999) 285.
[5] P. Vidmar, P. Fornasiero, J. Kašpar, M. Graziani, J. Catal. 171 (1997) 160.
[6] A. Trovarelli, Catalysis by Ceria and Related Materials, Imperial College Press, London, 2001.
[7] L.F. Liotta, A. Longo, A. Macaluso, A. Martorana, G. Pantaleo, A.M. Venezia, G. Deganello, Appl. Catal. B: Environ. 48 (2004) 133.
[8] S. Bernal, J.J. Calvino, M.A. Cauqui, J.M. Gatica, C. Larese, J.A.P. Omil, J.M. Pintado, Catal. Today 50 (1999) 175.
[9] A. Holmgren, F. Azarnoush, E. Fridell, Appl. Catal. B: Environ. 22 (1999) 49.
[10] S. Damyanova, J.M.C. Bueno, Appl. Catal. A: Gen. 253 (2003) 135.
[11] C. Bozo, N. Guilhaume, J.-M. Herrmann, J. Catal. 203 (2001) 393.
[12] Y.J. Mergler, A. van Aalst, J. van Delft, B.E. Nieuwenhuys, Appl. Catal. B: Environ. 10 (1996) 245.
[13] X. Wu, L. Xu, D. Weng, Appl. Surf. Sci. 221 (2004) 379.
[14] A.E. Nelson, K.H. Schulz, Appl. Surf. Sci. 210 (2003) 212.
[15] B.K. Cho, J. Catal. 131 (1991) 74.
[16] F.B. Noronha, E.C. Fendley, R.R. Soares, W.E. Alcarez, D.E. Resasco, Chem. Eng. J. 82 (2001) 25.
[17] A. Talo, J. Lahtinen, P. Hautojärvi, Appl. Catal. B: Environ. 5 (1995) 221.
[18] D. Briggs, M.P. Seah (Eds.), Practical Surface Analysis. Auger and X-Ray Photoelectron Spectroscopy, Appendix 6, vol. 1, Wiley, New York, 1990 .
[19] J. Fan, X. Wu, R. Ran, D. Weng, Appl. Surf. Sci. 245 (2005) 162.
[20] D.R. Mullins, K.Z. Zhang, Surf. Sci. 513 (2002) 163.
[21] A. Bourane, S. Derrouiche, D. Bianchi, J. Catal. 228 (2004) 288.
[22] V. Perrichon, L. Retailleau, P. Bazin, M. Daturi, J.C. Lavalley, Appl. Catal. A: Gen. 260 (2004) 1.
[23] J.E. Beson, M. Boudart, J. Catal. 4 (1965) 7042720.
[24] O. Stonehart, J. Appl. Electrochem. 112 (1992) 9952105.
[25] F. Zaera, Prog. Surf. Sci. 69 (2001) 1.
[26] J.L. Gland, D.A. Fischer, S. Shen, F. Zaera, J. Am. Chem. Soc. 112 (1990) 5695.
[27] A. Tschöpe, W. Liu, M. F-Stephanopoulos, J.Y. Ying, J. Catal. 157 (1995) 42.
[28] G.R. Rao, P. Fornasiero, R. Di Monte, J. Kašpar, G. Vlaic, G. Balducci, S. Meriani, G. Gubitosa, A. Cremona, M. Grazianiy, J. Catal. 162 (1996) 162.
[29] F.B. Passos, E.R. de Oliveira, L.V. Mattos, F.B. Noronha, Catal. Today 101 (2005) 23.
[30] S.E. Golunski, H.A. Hatcher, R.R. Rajaram, Appl. Catal. B: Environ. 5 (1995) 369.
[31] J.C. Frost, Nature 334 (1988) 577.
[32] L.N. Ikryannikova, G.L. Markaryan, A.N. Kharlanov, E.V. Lunina, Appl. Surf. Sci. 207 (2003) 100.